




FireFly: An Insect-Scale Aerial Robot Powered by Electroluminescent Soft Artificial Muscles

Suhan Kim , Yi-Hsuan Hsiao , YuFan Chen, Jie Mao, and YuFeng Chen , *Member, IEEE*

Abstract—Light production in natural fireflies represents an effective and unique method for communication and mating. Inspired by bioluminescence, we develop a 650 mg aerial robot powered by four electroluminescent (EL) dielectric elastomer actuators (DEAs) that have distinct colors and patterns. To enable simultaneous actuation and light emission, we embed EL particles in a DEA that has highly transparent electrodes. During robot flight, a strong (>40 V/ μm) and high frequency (400 Hz) electric field is generated within the DEA, exciting the EL particles to emit light. Compared to a regular DEA, our new design and fabrication methods require small additional weight (2.4%) and actuation power (3.2%) without adversely impacting the DEA's output power or lifetime. We further develop a position and attitude tracking method using vision-based color detection. We demonstrate a series of closed-loop flights and compare camera-tracked results with that of the state-of-the-art Vicon motion tracking system. The root-mean-square (rms) position and attitude errors are 2.55 mm and 2.60° , respectively. This work illustrates a novel and effective design for communication and motion tracking in extreme payload-constrained microscale aerial systems, and it further shows the potential of achieving coordinated swarm flights without using well-calibrated indoor tracking systems.

Index Terms—Micro/nano robots, soft robot materials and design, biologically-inspired robots, biomimetics, mechanism design.

I. INTRODUCTION

IN addition to demonstrating exquisite flight abilities, aerial insects exhibit complex behaviors such as feeding, evading predators, communication, and pollination. Fireflies (*Lampyridae*) are a family of insects that utilize bioluminescence for achieving unique functions. For instance, some species emit light to warn off predators while others attract preys [1]. Light emission is also an effective method for mating and communication [2], further leading to emergent swarm behaviors such

Manuscript received February 22, 2022; accepted May 21, 2022. Date of publication June 1, 2022; date of current version June 9, 2022. This letter was recommended for publication by Associate Editor J. Yu and Editor X. Liu upon evaluation of the reviewers' comments. This work was supported by the Research Laboratory of Electronics (RLE) at MIT, under the Research Support Committee Grant 2244181. (Corresponding authors: Yufeng Chen; Jie Mao.)

Suhan Kim, Yi-Hsuan Hsiao, YuFan Chen, and YuFeng Chen are with the Research Laboratory of Electronics, Department of Electrical Engineering and Computer Science, Massachusetts Institute of Technology (MIT), Cambridge, MA 02139 USA (e-mail: suhank@mit.edu; yhsiao@mit.edu; chenylf2@mit.edu; yufengc@mit.edu).

Jie Mao is with the State Key Laboratory of High-efficiency Utilization of Coal and Green Chemical Engineering, School of Chemistry and Chemical Engineering, Ningxia University, Yinchuan 750021, China (e-mail: maojie@nxu.edu.cn). Digital Object Identifier 10.1109/LRA.2022.3179486

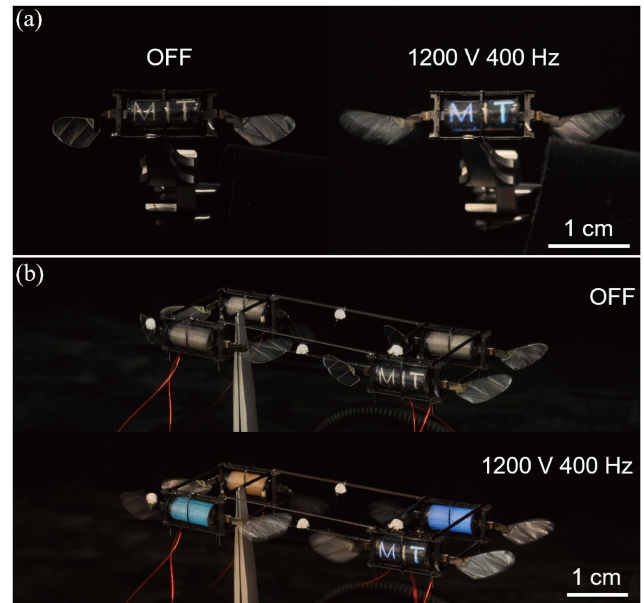


Fig. 1. A sub-gram aerial robot powered by ELDEAs. (a) One ELDEA is patterned with three letters “MIT”, and each letter emits a different color when the ELDEA is driven at 1200 V and 400 Hz. (b) Four different colored or patterned ELDEAs are installed in a 650 mg flapping wing robot. The robot emits light when it operates at hovering flight conditions.

as synchronous flashing [2]. Bioluminescent signaling is energy efficient as it only requires 1.6–3.4% of the insect’s metabolic expenditure [3].

Enabling insect-like functions in at-scale robots poses substantial engineering challenges in design, fabrication, sensing, and control. Over the past decade, numerous sub-gram aerial robots [4]–[7] were developed to demonstrate liftoff and hovering flights. Despite having a severely limited payload, these robots achieved versatile functions such as multimodal locomotion [8], [9], perching [10], onboard sensing [11], and light-powered takeoffs [12], [13]. Recently, we developed a novel class of aerial robots [14]–[16] powered by dielectric elastomer actuators (DEAs). Advances in fabrication processes reduced the robot hovering voltage to 500 V and increased the robot lift-to-weight ratio to 3.7:1 [14]. In addition, these resilient soft actuators enabled new demonstrations such as collision recovery and agile somersaults [16]. Achieving these insect-like flight capabilities illustrates the unique advantage of aerial robots driven by muscle-like soft actuators.

In this work, we present a firefly-inspired, 650 mg aerial robot (Fig. 1) that emits light during hovering flight. While the overall robot design is based on previous studies [14]–[16], we develop novel fabrication processes that enable simultaneous light emission and high-bandwidth (400 Hz) actuation. The new electroluminescent (EL) DEAs demonstrate similar robot flight performance without requiring substantially more power, adding robot weight, or reducing robot lifetime. Enabling light emission without impacting microrobot performance represents a major challenge because of four factors: 1) EL particles such as zinc sulphate (ZnS) require a strong and high frequency electric field; 2) light emission requires conductive and highly transparent electrodes; 3) mixing EL particles in the elastomer can adversely affect DEA mechanical and electrical behaviors; and 4) an aerial robot has a limited payload and it cannot have a dedicated EL layer. In existing EL displays [17]–[19], sensors [20], and robots [21], an elastomer-electrode layer is made for light emission and this adds substantial weight to the system. In addition, it requires a high voltage and high frequency driving signal that leads to high power consumption and low luminous efficacy ($43 \text{ mlm } W^{-1}$) [20]. We resolve this challenge by embedding EL particles in high bandwidth DEAs that actuate at 400 Hz during robot flight. This design enables simultaneous actuation and light emission using the same driving signal and it does not require additional robot components. Consequently, it only adds 2.4% of net robot weight and consumes an extra 3.2% of power at hovering flight conditions. Through experimentally characterizing DEAs’ mechanical and electrical behaviors under the addition of EL particles, we improve ELDEA designs to ensure the robot performance (maximum lift and lifetime) remains unchanged.

Furthermore, enabling light emission benefits the tracking and control of sub-gram aerial robots. Existing studies use an infrared motion capture system [4], [6], [9] for achieving closed-loop feedback control. The system emits infrared radiation, which bounces off reflective markers mounted on the aerial robots, and then it is detected by high-speed infrared cameras. This system imposes several limitations: 1) it requires heavy cameras ($>1 \text{ kg}$) that can emit and detect infrared radiations; 2) it requires well-controlled in-door environments without heat-emitting sources; and 3) it requires multiple markers mounted on the robot for position and attitude tracking. In contrast, active light emission allows motion tracking using miniaturized cameras that are receptive to visible light. We develop a fabrication process in which each DEA exhibits a different color or pattern (Fig. 1(b)). This design makes each DEA a unique active marker for visual tracking. In this work, we demonstrate closed-loop flights using a sub-gram robot powered by four ELDEAs (Fig. 1(b)). The robot position and attitude are tracked through both a Vicon motion tracking system and a set of three smartphone cameras. Compared to the Vicon system, visual tracking shows a root-mean-square (rms) position and attitude error of 2.55 mm and 2.60° , respectively. This result shows the potential of using commercially-available microscale cameras for enabling closed-loop flights. It further opens the opportunity for enabling coordinated swarm flights in sub-gram aerial robots.

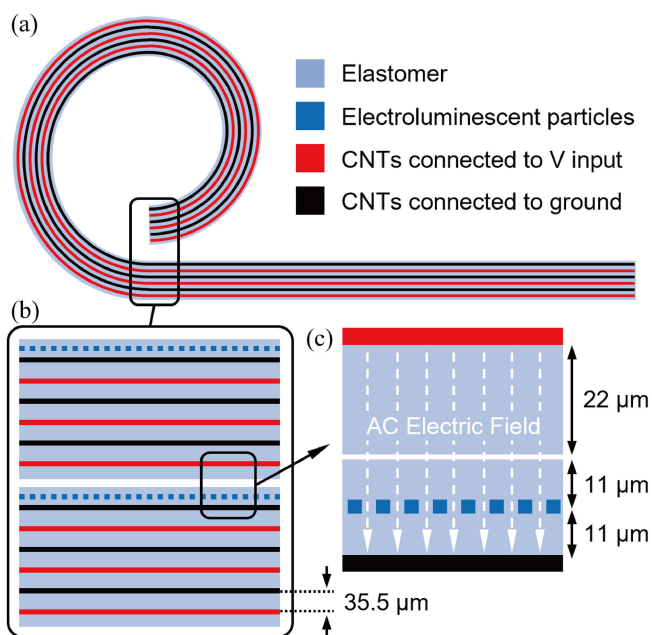


Fig. 2. Design of multiple-layered ELDEAs. (a) A $220 \mu\text{m}$, multiple-layered elastomer-electrode composite is rolled into a cylindrical shell. (b) An inset of (a) that shows the top elastomer layer is embedded with EL particles. (c) An inset of (b) that shows an alternating electric field between the top and bottom electrodes excites the EL particles to emit light.

II. DESIGN AND FABRICATION OF AN ELDEA

A. Design of a Multiple-Layered ELDEA

We design an ELDEA for driving soft aerial robots, which require power dense and lightweight flight muscles. A typical DEA is made of a soft elastomer layer sandwiched by a pair of compliant electrodes. When a voltage is applied across the electrodes, electrostatic stress causes the device to actuate. To reduce the operating voltage, previous studies [14], [22] developed multiple-layering techniques in which a DEA consists of many thin elastomer layers sandwiched by alternating electrodes. In this work, we roll a multiple-layered DEA into a cylindrical shell (Fig. 2(a)) for driving the robot.

To achieve electroluminescence in DEAs, we add EL particles such as ZnS into the elastomer layer. During actuation, the induced electric field excite EL particles to emit light, which shines through the highly transparent carbon nanotubes (CNTs) electrodes. There are two unique challenges in designing ELDEAs for high power applications such as flight. First, mixing solid particles (e.g., ZnS) in the elastomer layer reduces the dielectric breakdown voltage [23]. This can reduce an ELDEA’s maximum output power and adversely affect flight performance. Second, light emission requires a strong and high frequency driving electric field [23]. Previous works [20] separated the luminescence layer with other actuation and sensing layers. This traditional design would add weight to an actuator and require an extra control signal and substantially more power for light emission. These tradeoffs are detrimental to a robot’s flight performance.

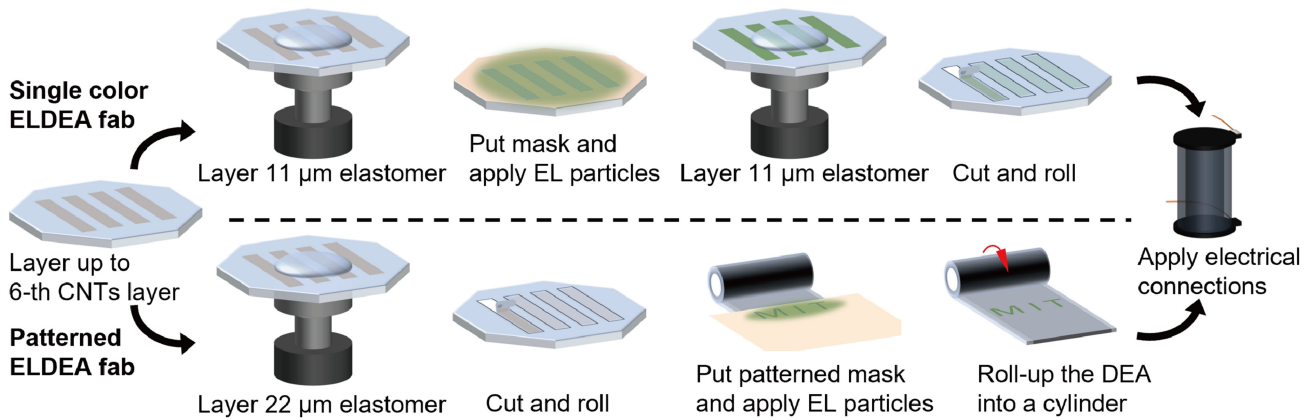


Fig. 3. Fabrication methods for single-colored and patterned ELDEAs. The top row illustrates the fabrication processes for making single-colored ELDEAs. A layer of EL particles is embedded between two $11\ \mu\text{m}$ thick elastomer layers through spin-coating. The single-colored ELDEA can be made efficiently and yield consistent luminance. The bottom row illustrates the steps for making a patterned ELDEA. During the rolling process, a patterned mask is put on top of the elastomer so EL particles are applied on uncovered areas. Patterned ELDEAs exhibit custom patterns and multiple colors, which are advantageous for robot identification in a swarm.

We address these challenges by optimizing the multiple-layering design of a rolled DEA and enabling simultaneous actuation and light emission. In our multiple-layering design, the DEA consists of an even number of electrodes so the top and bottom electrodes have opposite polarities. In the rolling process (Fig. 2(b)), the top and bottom elastomer layers form a new actuation layer in which an electric field is generated (Fig. 2(c)). We embed EL particles (Fig. 2(c)) in the top elastomer layer so the DEA can emit light during actuation. Our DEA has a high operating frequency (400–500 Hz) and it can withstand a strong electric field (40–60 V/ μm). These operating conditions ensure that the DEA actuation signal is suitable for simultaneous light emission. To account for the reduction of dielectric strength in the ELDEA’s top elastomer layer, we increase the thicknesses of the combined top and bottom layer accordingly. Fig. 2(b)–(c) shows the thicknesses of an intermediate layer and the combined EL layer are $35.5\ \mu\text{m}$ and $44\ \mu\text{m}$, respectively. The EL layer is 25% thicker than intermediate layers, and this design compensates for the 20% reduction of dielectric strength (see section III for experimental validation). For a 6-layer ELDEA, this design only leads to an 3% increase of net actuator weight.

B. Fabrication Methods for Embedding EL Particles

We develop fabrication methods for producing two types of ELDEAs that emit either a single-colored light or multiple-colored light with customized patterns. The fabrication methods are based on our prior works [14], [15] in which we sequentially stack elastomer (Elastosil P7670) and carbon nanotube electrode (Invisicon 3500, Nano-C Inc) layers to make a DEA. In this work, we make ELDEAs with 6 electrode and 7 elastomer layers. The EL particles are either embedded in or placed above the top elastomer layer.

To make a single-colored ELDEA, we embed EL particles in the top elastomer layer after completing all intermediate layers. The top row of Fig. 3 illustrates this fabrication process. First, we make an $11\ \mu\text{m}$ thin film through spin coating (5000 rpm). Then

we apply EL particles on the cured surface and pour uncured elastomer on top. Next, we use the same spin coating process to spread the elastomer and EL particles. We find the amount of embedded EL particles is inversely proportional to the spin coating speed and independent of the quantity placed on the elastomer prior to spin coating. Since we make four ELDEAs in one batch, this process is scalable and yields good consistency (measured in net luminance) among different samples.

Alternatively, we can fabricate a multiple-colored and patterned ELDEA through manually adding the EL particles during the rolling process. As illustrated in the bottom row of Fig. 3, a patterned mask is placed on the top elastomer layer after all the layering steps complete. Next, different EL particles are manually applied on different parts of the mask to customize patterns and colors. Finally, the ELDEA is rolled into a cylindrical shell and installed into a robot. This method is advantageous in producing ELDEAs of multiple colors and custom patterns. In future applications that involve flights of multiple micro-aerial-robots, multi-colored ELDEAs with unique patterns can be used to distinguish each individual robot in a swarm. However, it requires manual application of EL particles for each ELDEA and it has higher variability in the amount of applied EL particles.

III. CHARACTERIZATION OF ELDEA AND ROBOT PERFORMANCE

A. Luminance, Spectrum, and Dielectric Breakdown Measurement

We perform experiments to characterize EL properties and optimize ELDEA designs. First, we fabricate 2-layer ELDEA samples and measure luminance as functions of driving voltage and frequency. These ELDEA samples consist of a $44\ \mu\text{m}$ elastomer layer sandwiched by 2 electrode layers. For making the green, blue, and orange samples, we put 3 mg of the corresponding EL particles and use the same spin coating speeds (5000 rpm) for each sample set. Next, we place a luminance meter (TES-137) on each unrolled sample and measure the

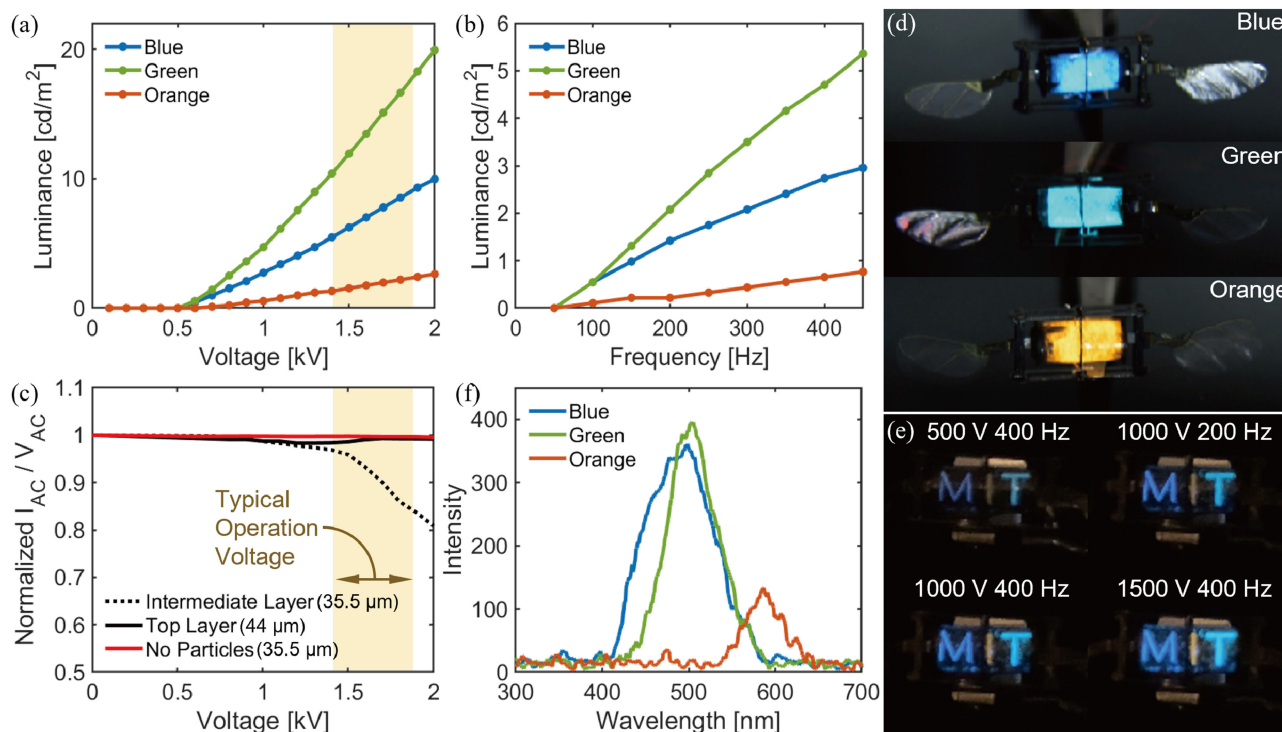


Fig. 4. Characterization of ELDEAs. (a-b) Measured luminance as functions of driving voltage (a) and frequency (b). (c) An ELDEA's dielectric breakdown voltage reduces due to the addition of EL particles. To maintain an ELDEA's performance, the top elastomer layer thickness is increased by 25%. (d) Images of the blue, green, and orange ELDEAs operating at flight conditions. (e) An image sequence that shows luminance increases as driving frequency and voltage increase. (f) Measured spectra of the blue, green, and orange ELDEAs. The y-axis represents the number of photons detected in a 5-second duration at a particular wavelength in the interval of ± 1 nm.

luminance at different operating conditions. Fig. 4(a) compares the luminance of each sample when the driving voltage varies from 0 to 2 kV. In these experiments, the driving frequency is fixed at 400 Hz. We observe the luminance varies approximately quadratically as the driving voltage increases. Fig. 4(b) illustrates the samples' frequency response when the driving voltage is fixed at 1 kV. We observe the sample luminance increases linearly as a function of driving frequency. Fig. 4(a)–(b) further shows different colored EL particles exhibit different luminance under the same fabrication and driving conditions.

Next, we investigate the influence of EL particles on dielectric strength reduction. The embedded solid particles reduce elastomer homogeneity and create defects such as microscopic air bubbles. Consequently, early dielectric breakdown occurs and this reduces DEA performance. To characterize this effect, we compare the dielectric properties of two 35.5 μm thick samples with or without EL particles. Here the sample thickness is chosen as the DEA's intermediate layer thickness. The red line in Fig. 4(c) shows the sample without embedded particles maintains constant conductance in the 0–2 kV driving range. Based on our prior work [14], this implies the sample does not experience self-clearing which would reduce conductance. In contrast, the dotted line shows the sample with EL particles experiences a substantial reduction of conductance, which implies self-clearing occurs due to early dielectric breakdown. To mitigate this issue, we increase the sample thickness by 25% to reduce the effective electric field. The solid black line

in Fig. 4(d) shows the 44 μm thick sample does not suffer a reduction of conductance at high driving voltages. Based on this result, we set the top layer thickness of our ELDEA to 44 μm .

Finally, we make 4 ELDEAs (Fig. 4(d)–(e)) and measure their spectra. Fig. 4(d) shows the blue, green, and orange ELDEAs operating at robot flight conditions. Fig. 4(e) shows a three-colored ELDEA with the pattern “MIT”. The ELDEA brightness increases as driving frequency and voltage increase. This experiment is also shown in Supplementary Video 1. We further measure the spectra (Fig. 4(f)) of the blue, green, and orange ELDEAs using a spectrometer (HR4000CG-UV-NIR, Ocean Optics). The blue and green ELDEAs exhibit similar spectra, with peak intensities in the 490–510 nm range. The orange ELDEA shows a peak intensity at 590 nm, but its brightness is lower than the other ELDEAs. For all four ELDEAs, light emission becomes visible to naked eyes and cameras when the driving voltage and frequencies exceed 500 V and 400 Hz. At the same driving condition, the ELDEA is brighter than a flat test sample because it is rolled into an overlapping cylindrical shell. These experiments show the ELDEAs can emit bright and distinguishable colors when operated at flight conditions. While these measurements are conducted in a dim environment, we also conduct experiments in bright environments. We find the ELDEA colors are detectable to a smartphone camera when environmental brightness is up to 125 cd m^{-2} (1.7 times of typical indoor illumination).

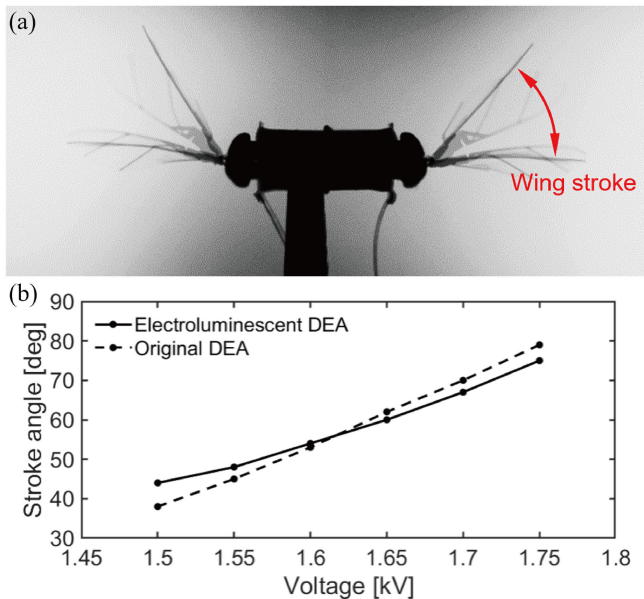


Fig. 5. Characterization of robot performance. (a) A robot module is driven at 400 Hz and 1500 V. The robot’s wing stroke amplitude is proportional to the time-averaged lift force generation. (b) Comparison of two robots’ stroke motion as functions of driving voltage. The experiments show the ELDEA-driven robot generates similar flapping kinematics, which implies it produces similar net lift force.

TABLE I
COMPARISON OF ELDEA AND ORIGINAL DEA

Metric	Weight	R	C	Power	Endurance
Unit	mg	k Ω	nF	W	Cycles
ELDEA	125	71.4	1.76	0.72	$> 2 \times 10^6$
Original DEA	122	70.8	1.74	0.70	$> 2 \times 10^6$

B. Robot Performance Measurement

To evaluate ELDEA performance, we install the actuator into a 155 mg flapping-wing robot and conduct static flapping experiments. Fig. 5(a) shows a composite image that illustrates a robot’s flapping-wing motion at the operating condition of 1500 V and 400 Hz. Based on our prior works [14]–[16], a robot’s net lift force is proportional to its wing stroke amplitude. Fig. 5(b) compares the wing stroke motion of two robots with or without embedded EL particles. In these experiments, both robots are driven at 400 Hz while the driving voltage increases from 1.5 kV to 1.75 kV. Both robots show similar flapping kinematics, which imply they produce similar aerodynamic forces. These static flapping experiments further suggest the ELDEA-driven robot can achieve a similar level of flight performance.

Furthermore, we find these two actuators have similar weight, electrical properties, and lifetime. Table I shows the ELDEA is 2.4% heavier than the DEA without EL particles. These actuators can be modeled as a series RC load. We measure their resistances and capacitances using a custom circuit and find these values are within 2% of each other. Their electrical power dissipation is also within 3.2%, showing the two actuators exhibit similar electrical and mechanical properties. Finally, both actuators can be driven for over 2 million cycles (correspond

to over 80 minutes of cumulative operation) at the robot flight condition. These experiments imply that light emission does not adversely influence the robot flight performance. We construct four robot modules powered by the four ELDEAs shown in Fig. 4(d)–(e). Then we assemble them into a 650 mg robot (Fig. 6(a)) to demonstrate closed-loop flights.

IV. FLIGHT AND TRACKING DEMONSTRATION

We perform a sequence of closed-loop flights (Supplementary Videos 2-4) using a four-ELDEA-driven robot named FireFly. In these flights, a motion capture system (6 Vicon Vantage V5 cameras) provides position and attitude tracking at 420 Hz. Based on a previous work [15], we implement a custom flight controller that runs at 10 kHz in the MATLAB Simulink environment. In addition, we demonstrate the ELDEAs can enable vision-based trajectory reconstruction using smartphone cameras. Vision-based cameras can detect different colored light emitted from each ELDEA, and this can be used to calculate robot position and attitude. Compared to computer vision strategies that detect passive robot features, our method requires less computation because each ELDEA represents a distinct active feature.

A. Experimental Setup and Visual Tracking Design

To film the robot flights, we use one high speed camera (Phantom V710) and three smartphone cameras (Fig. 6(b)). Fig. 6(c)–(f) shows a 5-second flight seen by each of the four cameras. We use the three smartphone cameras to reconstruct the robot’s trajectory and attitude during flight. The reconstructed flight trajectory of this experiment will be presented and analyzed in Figs. 7 and 8. The same flight experiment is also shown in Supplementary Video 2.

First, we adapt an existing method [24] for camera calibration. A camera can be modeled mathematically using projective geometry, where a point $\mathbf{X} \in R^3$ along a line in 3D is mapped to a pixel $\mathbf{x} \in R^2$ in the image space, that is $\mathbf{x} = \pi(\mathbf{X})$. We adapt a pinhole camera model, where the projection operation π can be represented by a pair of matrices, that is $\mathbf{x} = \mathbf{K}[\mathbf{R}|\mathbf{t}]\mathbf{X}$, where \mathbf{K} , \mathbf{R} , and \mathbf{t} represent the camera’s intrinsic (e.g., focal length, principal point) and extrinsic parameters (e.g., relative rotation and translation). For each of the three smartphone cameras, we first estimate the camera’s intrinsic parameters by finding the projection \mathbf{x}_i of a known calibration object \mathbf{X}_i . Then, we estimate each camera’s extrinsic parameters using the PnP algorithm [24] given the coordinates of a set of known points in 3D. In this work, we calibrate the smartphone cameras against the Vicon system for ease of comparison.

Next, we implement a tracking algorithm that extracts the DEA pixel positions \mathbf{x}_{ij} in each camera. First, the code removes the common background through median filtering. For each frame, our code identifies the green, orange, and blue DEAs based on their distinct colors. A DEA’s centroid position is calculated as the geometric centroid of each colored region. The algorithm predicts the location of the patterned DEA based on the positions of the first three DEAs, and then applies a black mask that covers the first three DEAs. Following this step, the code refines the centroid position of the fourth DEA through

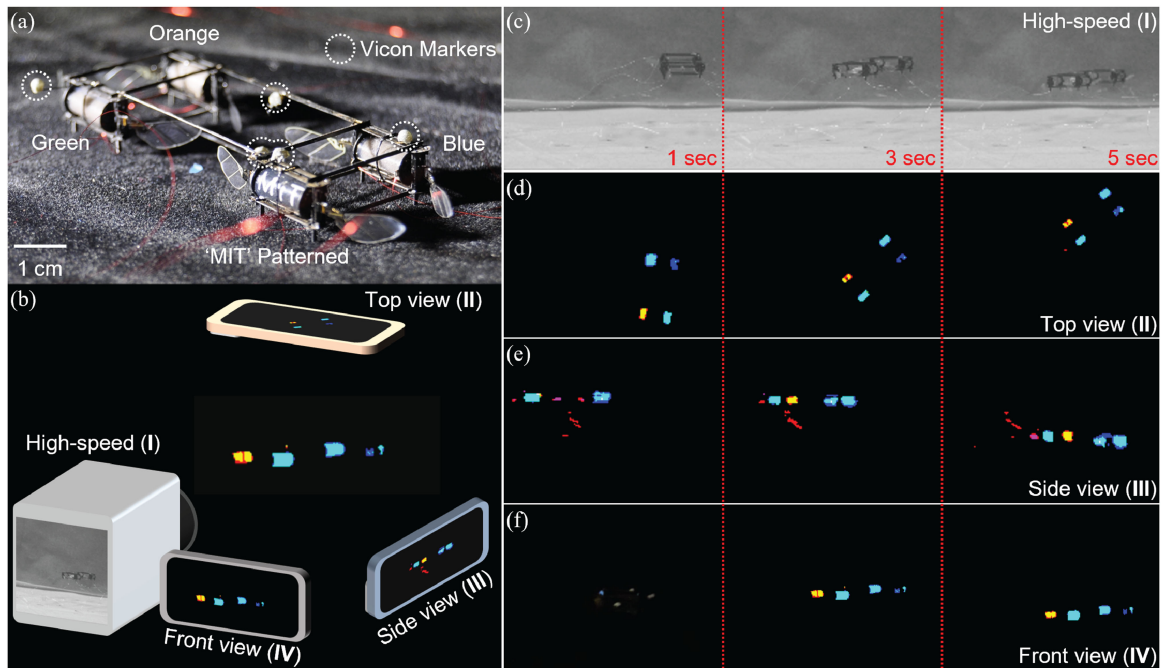


Fig. 6. A 5-second closed-loop flight demonstration. (a) A 650 mg robot that is equipped with four different colored or patterned ELDEAs. The robot has five reflective markers for real-time motion tracking and feedback control. (b) This flight is recorded by a high-speed camera and three smartphone cameras. (c-f) Image sequences that show the robot flight from the perspective of the high-speed camera (c), top (d), side (e), and front (f) view cameras.

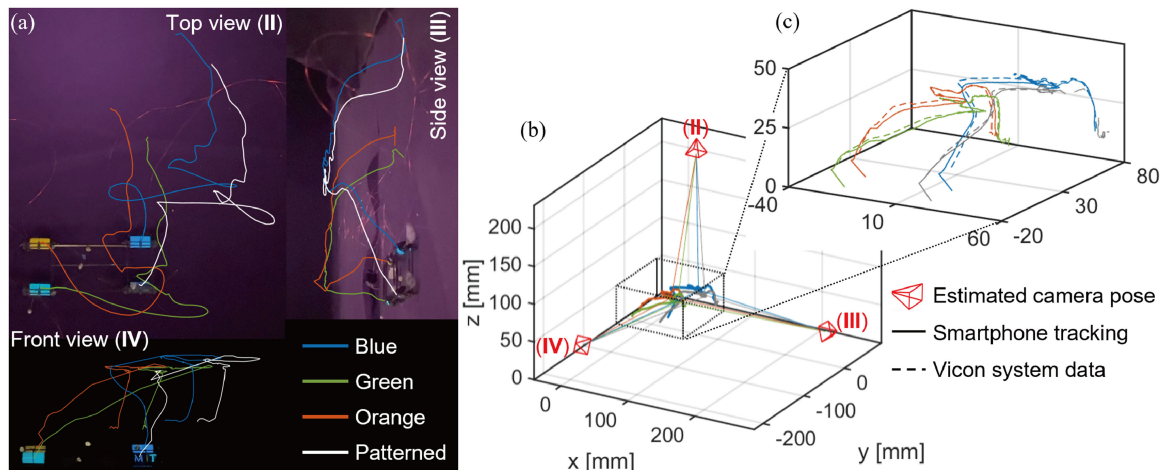


Fig. 7. Automated tracking and trajectory reconstruction based on the smartphone videos. (a) Automated tracking of the four ELDEAs in the top, side, and front view videos. (b) Camera pose calibration and reconstructed 3D trajectories of each ELDEA. (c) An inset graph of (b) that compares the vision-tracked trajectories with that from the Vicon motion tracking system.

identifying all three colors in the vicinity region (correspond to each of the three letters in “MIT”) and calculating the geometric centroid. This method calculates every DEA centroid positions $\mathbf{x}_{ij} = (u_{ij}, v_{ij})$ in each camera view, where $i \in 1, 2, 3, 4$ and $j \in 1, 2, 3$ denote the DEA and the camera indices, respectively.

From the 2D keypoints in the image plane, we further reconstruct each DEA’s 3D position relative to the global coordinate system. Each DEA’s 3D position \mathbf{X}_i can be found individually by minimizing the reprojection error, $\sum_j \|\mathbf{x}_{ij} - \pi_j(\mathbf{X}_i)\|_2$ with respect to all of the cameras. More precisely, each detection $\mathbf{x}_j = (u_j, v_j)$ represents a ray \mathbf{r}_j starting from the camera center

\mathbf{C}_j going through \mathbf{x}_j in the image plane. Thus, we formulate an optimization problem to find the closest approach between this set of detection rays,

$$\arg \min_{\lambda_j} \sum_{j=1}^3 \sum_{k>j}^3 \|\mathbf{C}_j + \lambda_j \mathbf{r}_j - \mathbf{C}_k - \lambda_k \mathbf{r}_k\|_2 \quad (1)$$

where λ_j is a scalar variable that determines the distance along the j^{th} ray. Finally, we can retrieve the DEA’s 3D position by finding the average of $\mathbf{C}_j + \lambda_j \mathbf{r}_j$. This is a quadratic equation

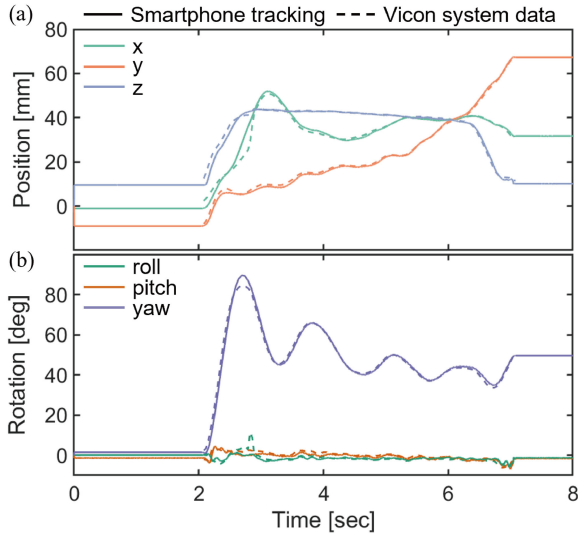


Fig. 8. Comparison of robot position and attitude tracking based on smartphone cameras and the Vicon system. (a-b) Robot COM position (a) and attitude (b) during a 5-second closed-loop flight. The solid and dotted lines represent smartphone and Vicon tracking results, respectively.

with an analytical solution that permits efficient computation in real time.

Finally, we compute the robot's position and attitude based on the four DEAs' tracked positions. The robot center of mass position is calculated as the mean actuator position:

$$\mathbf{X}_{centroid} = \frac{1}{4} \sum_{i=1}^4 \mathbf{X}_i \quad (2)$$

To calculate the robot attitude, we first formulate a rotation matrix based on the roll (θ_x), pitch (θ_y), and yaw (θ_z) convention:

$$\mathbf{R}(\theta_x, \theta_y, \theta_z) = \begin{bmatrix} C_y C_z & -C_y S_z & S_y \\ C_x S_z + S_x S_y C_z & C_x C_z - S_x S_y S_z & -S_x C_y \\ S_x S_z - C_x S_y C_z & S_x C_z + C_x S_y S_z & C_x C_y \end{bmatrix} \quad (3)$$

Here S_i and C_i denote $\sin \theta_i$ and $\cos \theta_i$, respectively. The values of θ_x , θ_y , and θ_z are calculated through minimizing the sum of differences between the tracked DEA to centroid distance and the calculated distances through the rotation matrix \mathbf{R} . The objective function is given by:

$$\arg \min_{\theta_x, \theta_y, \theta_z} \sum_{i=1}^4 \|(\mathbf{X}_i - \mathbf{X}_{centroid}) - \mathbf{R}(\theta_x, \theta_y, \theta_z) \mathbf{D}_i\|_2 \quad (4)$$

where $\mathbf{D}_i \in \mathbb{R}^3$ is the position of the i^{th} DEA relative to the robot COM in the robot coordinate system.

B. Flight Result and Tracking Comparison

We perform three 5-second flights and use one flight result for comparing the tracking methods. Fig. 7(a) shows the tracked trajectory of each DEA in the top, side, and front view cameras. The estimated camera positions and poses (red) are shown in

Fig. 7(b). Based on these 2D results and our trajectory reconstruction algorithm, we further calculate the 3D trajectory of each DEA (Fig. 7(b)). Fig. 7(c) shows an inset of 7(b) in which we overlay the Vicon tracked trajectories (dotted lines) on the trajectories (solid lines) tracked by smartphone cameras. Compared to Vicon tracked results, the vision-based reconstruction has a rms and maximum error of 2.9 mm and 12.4 mm, respectively. This corresponds to 7.3% and 31% of the robot's body length. Supplementary Video 3 illustrates the result of vision-based motion tracking.

In addition, we use the four DEA trajectories to calculate robot COM position and attitude. As shown in Fig. 8 a, the vision-based COM reconstruction matches well with the Vicon tracked robot positions. Treating the Vicon tracked result as ground truth, we find the rms and maximum vision-tracked errors are 2.55 mm and 10.6 mm, respectively. Furthermore, Fig. 8(b) compares the robot attitude based on Vicon tracking and camera reconstruction. The rms and maximum errors are 2.60° and 10.9° , respectively. In most part of the flight duration, vision-based tracking matches closely with the Vicon tracking results. The tracking quality becomes worse during takeoff and landing when some ELDEAs are occluded from the side or front view cameras. Future work can incorporate motion prediction in the tracking algorithm to compensate for temporary loss of tracking. These results demonstrate the ELDEA-driven FireFly can achieve closed-loop flight and enable vision-based tracking. This has the potential to replace the Vicon system during future closed-loop flights. Supplementary Video 4 shows three repeated flights to demonstrate the robot performance does not deteriorate over short flight duration. In these flights, the robot has no yaw control and weak position control so it drifts near the position set point. This controller design helps us to compare Vicon and vision-based trajectory tracking.

V. CONCLUSION

In this study, we develop a 650 mg light-emitting soft aerial robot that is powered by four power dense and long endurance ELDEAs. We present design and fabrication methods that enable simultaneous actuation and light emission in an extreme payload-limited microscale system. Similar to natural fireflies, our robot only spends small additional power (3.2%) for emitting light during flight. Our ELDEA design adds 2% weight to the robot and it maintains similar actuator power density, bandwidth, and endurance. We further demonstrate three 5-second flights in which we compare vision-based motion tracking with the state-of-the-art infrared tracking. Through using 3 smartphone cameras, we track the 3D positions of four ELDEAs with distinct colors or patterns. We reconstruct robot COM position and attitude based on the ELDEA positions. Compared to the Vicon tracking, the vision-based tracking have small rms position and attitude errors of 2.55 mm and 2.60° , respectively. This result shows the promise of implementing vision-based feedback control for light-emitting insect-scale robots.

More broadly, this work illustrates another advantage of agile, robust, and multifunctional soft robots. In prior works [14]–[16], our sub-gram soft-actuated aerial robot has demonstrated

hovering flights, collision sensing and recovery, and acrobatic somersaults. In this work, we enable light emission without compromising the robot flight performance. Many of these insect-like flight capabilities surpass the state-of-the-art rigid-powered microrobots due to the unique properties of power-dense, robust, long endurance, and multi-functional soft actuators. In future studies, we envision light emission can be crucial for enabling communication in coordinated swarm flights. For instance, a swarm of flying microrobots may emit and detect light to avoid collisions. If a microrobot collides with an obstacle or is stuck in a cluttered space, it can flash light at others as a warning signal. In the long term, we envision deploying a heterogeneous microrobotic swarm consisting of terrestrial and aerial robots. The terrestrial robots may each carry a small camera and collectively form a sensing network for tracking the aerial robots.

Despite demonstrating novel functions, this work has limitations that future studies need to address. First, the robot cannot control the emitted light intensity and color during flight. This is a design tradeoff because we aim to minimize the additional cost on power and control. Incorporating independent light emitting layers and control signals can enable future robots to flash selectively during flight. This is important for demonstrating synchronized flashing in swarm flight. In addition, there remains substantial work in realizing closed-loop flights via vision-based tracking feedback. Currently our smartphone cameras only film at 30 Hz and they are not synchronized with each other. In future flight experiments, we need to identify the minimum required tracking frequency for sub-gram aerial robots, synchronize tracking cameras, and implement efficient tracking algorithms that can run in real-time. We will also explore sensor fusion techniques where the robot relies on a combination of onboard sensors (e.g., gyroscopes [25], magnetometer [11]) and external vision-based tracking.

REFERENCES

- [1] J. E. Lloyd, "Aggressive mimicry in photuris: Firefly femmes fatales," *Science*, vol. 149, no. 3684, pp. 653–654, 1965.
- [2] J. F. Case, "Courting behavior in a synchronously flashing, aggregative firefly, *pteroptyx tener*," *Biol. Bull.*, vol. 159, no. 3, pp. 613–625, 1980.
- [3] W. A. Woods Jr, H. Hendrickson, J. Mason, and S. M. Lewis, "Energy and predation costs of firefly courtship signals," *Amer. Naturalist*, vol. 170, no. 5, pp. 702–708, 2007.
- [4] K. Y. Ma, P. Chirarattananon, S. B. Fuller, and R. J. Wood, "Controlled flight of a biologically inspired, insect-scale robot," *Science*, vol. 340, no. 6132, pp. 603–607, 2013.
- [5] D. S. Drew, N. O. Lambert, C. B. Schindler, and K. S. Pister, "Toward controlled flight of the ionocraft: A flying microrobot using electrohydrodynamic thrust with onboard sensing and no moving parts," *IEEE Robot. Automat. Lett.*, vol. 3, no. 4, pp. 2807–2813, Oct. 2018.
- [6] X. Yang, Y. Chen, L. Chang, A. A. Calderón, and N. O. Pérez-Arancibia, "Bee⁺: A 95-mg four-winged insect-scale flying robot driven by twinned unimorph actuators," *IEEE Robot. Automat. Lett.*, vol. 4, no. 4, pp. 4270–4277, Oct. 2019.
- [7] Y. Zou, W. Zhang, and Z. Zhang, "Liftoff of an electromagnetically driven insect-inspired flapping-wing robot," *IEEE Trans. Robot.*, vol. 32, no. 5, pp. 1285–1289, Oct. 2016.
- [8] Y. Chen *et al.*, "A biologically inspired, flapping-wing, hybrid aerial-aquatic microrobot," *Sci. Robot.*, vol. 2, no. 11, 2017, Art. no. eaao5619.
- [9] Y. M. Chukewad, J. James, A. Singh, and S. Fuller, "Robofly: An insect-sized robot with simplified fabrication that is capable of flight, ground, and water surface locomotion," *IEEE Trans. Robot.*, vol. 37, no. 6, pp. 2025–2040, Dec. 2021.
- [10] M. Graule *et al.*, "Perching and takeoff of a robotic insect on overhangs using switchable electrostatic adhesion," *Science*, vol. 352, no. 6288, pp. 978–982, 2016.
- [11] E. F. Helbling, S. B. Fuller, and R. J. Wood, "Pitch and yaw control of a robotic insect using an onboard magnetometer," in *Proc. IEEE Int. Conf. Robot. Automat.*, 2014, pp. 5516–5522.
- [12] N. T. Jafferis, E. F. Helbling, M. Karpelson, and R. J. Wood, "Untethered flight of an insect-sized flapping-wing microscale aerial vehicle," *Nature*, vol. 570, no. 7762, pp. 491–495, 2019.
- [13] J. James, V. Iyer, Y. Chukewad, S. Gollakota, and S. B. Fuller, "Liftoff of a 190 mg laser-powered aerial vehicle: The lightest wireless robot to fly," in *Proc. IEEE Int. Conf. Robot. Automat.*, 2018, pp. 3587–3594.
- [14] Z. Ren *et al.*, "A high-lift micro-aerial-robot powered by low-voltage and long-endurance dielectric elastomer actuators," *Adv. Mater.*, vol. 34, no. 7, 2022, Art. no. 2106757.
- [15] Y. Chen *et al.*, "Controlled flight of a microrobot powered by soft artificial muscles," *Nature*, vol. 575, no. 7782, pp. 324–329, 2019.
- [16] Y. Chen, S. Xu, Z. Ren, and P. Chirarattananon, "Collision resilient insect-scale soft-actuated aerial robots with high agility," *IEEE Trans. Robot.*, vol. 37, no. 5, pp. 1752–1764, Oct. 2021.
- [17] J. Wang, C. Yan, K. J. Chee, and P. S. Lee, "Highly stretchable and self-deformable alternating current electroluminescent devices," *Adv. Mater.*, vol. 27, no. 18, pp. 2876–2882, 2015.
- [18] F. Stauffer and K. Tybrandt, "Bright stretchable alternating current electroluminescent displays based on high permittivity composites," *Adv. Mater.*, vol. 28, no. 33, pp. 7200–7203, 2016.
- [19] P. Xie, J. Mao, and Y. Luo, "Highly bright and stable electroluminescent devices with extraordinary stretchability and ultraconformability," *J. Mater. Chem. C*, vol. 7, no. 3, pp. 484–489, 2019.
- [20] C. Larson *et al.*, "Highly stretchable electroluminescent skin for optical signaling and tactile sensing," *Science*, vol. 351, no. 6277, pp. 1071–1074, 2016.
- [21] Y. R. Lee *et al.*, "Electroluminescent soft elastomer actuators with adjustable luminance and strain," *Soft Matter*, vol. 15, no. 40, pp. 7996–8000, 2019.
- [22] M. Duduta, R. J. Wood, and D. R. Clarke, "Multilayer dielectric elastomers for fast, programmable actuation without prestretch," *Adv. Mater.*, vol. 28, no. 36, pp. 8058–8063, 2016.
- [23] D. Yang, M. Tian, Y. Dong, H. Kang, D. Gong, and L. Zhang, "A high-performance dielectric elastomer consisting of bio-based polyester elastomer and titanium dioxide powder," *J. Appl. Phys.*, vol. 114, no. 15, 2013, Art. no. 154104.
- [24] R. Hartley and A. Zisserman, *Multiple View Geometry in Computer Vision*. Cambridge, U.K.: Cambridge Univ. Press, 2003.
- [25] S. B. Fuller, E. F. Helbling, P. Chirarattananon, and R. J. Wood, "Using a mems gyroscope to stabilize the attitude of a fly-sized hovering robot," in *Proc. Int. Conf. Micro Air Vehicles*, 2014, Art. no. 44.